CMS Physics Analysis Summary

Contact: cms-phys-conveners-ftr@cern.ch 2022/03/16

Search for leptophobic Z′ resonances decaying to charginos in the dilepton plus missing transverse momentum final state at the HL-LHC

The CMS Collaboration

Abstract

The prospects of a search for a massive leptophobic Z′ decaying to a pair of charginos at the High Luminosity LHC at CERN is explored. The final state consists of two oppositely charged leptons and missing transverse momentum. The analysis is based on generated samples of proton-proton collision events at $\sqrt{s} = 14$ TeV interfaced to the Phase-2 CMS Delphes detector simulation. A deep neural network is used for signal extraction. The expected signal sensitivity for a Z′ with a narrow width is estimated. For an integrated luminosity of 3 ab^{-1}, Z′ masses up to 4.4 TeV are expected to be excluded.

1 Introduction

This note presents a search for leptophobic Z′ resonances decaying to charginos in the dilepton plus missing transverse momentum final state at the High Luminosity LHC (HL-LHC) with 14 TeV proton-proton collisions and with the Phase-2 CMS detector. The Phase-2 upgrade consists of replacements and improvements in the CMS detector systems to provide the optimal physics performance under the challenging conditions of the HL-LHC [1].

Searches for high mass resonances have been performed by ATLAS and CMS since the beginning of LHC data taking, and sensitivity projections have been studied for the HL-LHC. However, these searches mainly focus on direct resonance decays to standard model (SM) particles, in particular to dileptons and dijets [2–4]. Yet, well-motivated theoretical mechanisms also suggest scenarios where resonances decay into BSM particles. One example is the leptophobic Z′ resonances appearing within the context of the U(1)′-extended minimal supersymmetric standard model (UMSSM) scenario, which is derived from embedding SUSY in the unified gauge group E_6. The U(1)′ extension leads to an extra gauge boson Z′. In these scenarios, several mechanisms exist that achieve leptophobic Z′, where the Z′ decays to leptons are suppressed [5–7]. Z′ decays are instead dominated by other channels, including decays to SM final states with quark pairs, W^+W^-, hZ, neutrino pairs, or SUSY final states with electroweak gaugino pairs.

This study focuses on the case of a leptophobic Z′ decaying into two charginos, which in turn each decay into a leptonically decaying W boson and a neutralino, as shown in Figure 1. This process leads to a distinct signature with two oppositely charged high momentum leptons (e^+e^-, $\mu^+\mu^-$, $e^\pm\mu^\mp$) and high missing transverse momentum ($p_{\mathrm{T}}^{\mathrm{miss}}$). Leptophobic Z′ has not yet been explored or interpreted by any of the existing LHC searches, making the presented study the first example. The analysis is performed using Monte Carlo samples generated at 14 TeV center-of-mass energy and simulated with Phase-2 CMS detector conditions. The leptophobic Z' production has moderate cross sections. Moreover, in the full model scheme including the complete sparticle content with their theory-predicted properties, decays of Z' to charginos, in particular combined with the subsequent chargino decays to leptonically decaying W bosons both have small branching ratios of the order of few percent. Therefore, the increased luminosity of HL-LHC is highly relevant for sensitivity to such models. In order to extract signal from the highly dominant backgrounds, the analysis employs a multi-classifier deep neural network (DNN).

This document is organized as follows: After a brief introductions to the Phase-2 CMS detector and Monte Carlo (MC) event samples in Sections 2 and 3, Section 4 describes the analysis methodology, including object and event selection and DNN categorization. Section 5 will summarize the systematic uncertainties. The analysis results and Z′ interpretation will be given in Section 6 followed by conclusions in Section 7.

2 The Phase-2 CMS detector

The CMS detector [8] will be substantially upgraded in order to fully exploit the physics potential offered by the increase in luminosity, and to cope with the demanding operational conditions at the HL-LHC [1, 9–12]. The upgrade of the first level hardware trigger (L1) will allow for an increase of L1 rate and latency to about 750 kHz and 12.5 μs, respectively, and the high-level software trigger (HLT) is expected to reduce the rate by about a factor of 100 to 7.5 kHz. The entire pixel and strip tracker detectors will be replaced to increase the granularity, reduce the material budget in the tracking volume, improve the radiation hardness, and extend the

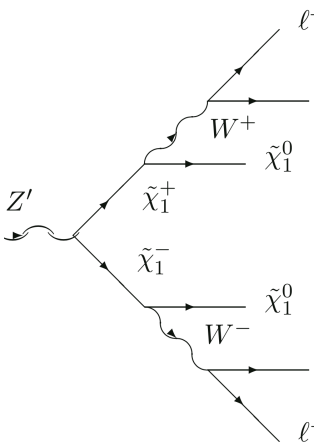

Figure 1: Feynman diagram showing the signal process in this analysis: leptophopbic Z′ decaying to two charginos, subsequently decaying to W and neutralino.

geometrical coverage and provide efficient tracking up to pseudorapidities of about $|\eta| = 4$. The muon system will be enhanced by upgrading the electronics of the existing cathode strip chambers (CSC), resistive plate chambers (RPC) and drift tubes (DT). New muon detectors based on improved RPC and gas electron multiplier (GEM) technologies will be installed to add redundancy, increase the geometrical coverage up to about $|\eta| = 2.8$, and improve the trigger and reconstruction performance in the forward region. The barrel electromagnetic calorimeter (ECAL) will feature the upgraded front-end electronics that will be able to exploit the information from single crystals at the L1 trigger level, to accommodate trigger latency and bandwidth requirements, and to provide 160 MHz sampling allowing high precision timing capability for photons. The hadronic calorimeter (HCAL), consisting in the barrel region of brass absorber plates and plastic scintillator layers, will be read out by silicon photomultipliers (SiPMs). The endcap electromagnetic and hadron calorimeters will be replaced with a new combined sampling calorimeter (HGCal) that will provide highly-segmented spatial information in both transverse and longitudinal directions, as well as high-precision timing information. Finally, the addition of a new timing detector for minimum ionizing particles (MTD) in both barrel and endcap regions is envisaged to provide the capability for 4-dimensional reconstruction of interaction vertices that will significantly offset the CMS performance degradation due to high number of proton-proton interactions per event, i.e. pileup.

A detailed overview of the CMS detector upgrade program is presented in Ref. [1, 9–12], while the expected performance of the reconstruction algorithms and pileup mitigation with the CMS detector is summarised in Ref. [13].

3 Monte Carlo event samples

The signal samples are generated at $\sqrt{s} = 14$ TeV for the exclusive process $pp \to Z' \to \tilde{\chi}_1^+\tilde{\chi}_1^- \to W^+\tilde{\chi}_1^0 W^-\tilde{\chi}_1^0 \to \ell^+\nu\tilde{\chi}_1^0\ell^-\nu\tilde{\chi}_1^0$ by MADGRAPH5_aMC@NLO (v2.6.5) at the leading order (LO) precision. The Z′ mass is scanned from 1.7 TeV to 4.1 TeV in steps of 400 GeV, while chargino mass is scanned from 345 GeV to 1.845 TeV in steps of 250 GeV, where neutralino mass is taken as half of the chargino mass. Events are generated in a theoretical framework with a narrow Z′ width, where the width is calculated to be approximately 1.5% of the Z′ mass, depending on the signal point. The width values are computed by MADGRAPH5_aMC@NLO. The effective cross sections are calculated by taking the $Z' \to \tilde{\chi}_1^+\tilde{\chi}_1^- \to W^+\tilde{\chi}_1^0 W^-\tilde{\chi}_1^0$ branching ratio to equal

1. Subsequent showering and hadronization is performed by PYTHIA 8. Background samples are produced by MADGRAPH5_aMC@NLO or POWHEG at parton level, with the showering and hadronization provided by PYTHIA 8. The background processes, cross sections and generators used are summarized in Table 1.

The parametrized fast simulation package DELPHES is used to simulate the CMS Phase 2 detector response on both the signal and background events, with an average of 200 pileup interactions per event.

Table 1: Background samples used in the analysis. The samples for which a decay channel are specified are generated exclusively for that decay, while the others are inclusive in decays.

Process	Cross section at 14 TeV (pb)	Generator
$t\bar{t} \to ll$	80.22	MADGRAPH5_aMC@NLO
DY+jets ($M_{\ell\ell} > 100\,\text{GeV}$)	246.5	MADGRAPH5_aMC@NLO
tW	84.4	POWHEG
$WZ(\to 3\ell + \nu) + 0\text{jets}$	3.125	MADGRAPH5_aMC@NLO
$WZ(\to 3\ell + \nu) + 1\text{jet}$	0.955	MADGRAPH5_aMC@NLO
$VV \to 2l + 2\nu$, $V = W, Z$	13.23	MADGRAPH5_aMC@NLO

4 Analysis method

The analysis considers final states with two opposite charge leptons and significant missing transverse momentum, and is performed in the ee, $\mu\mu$ and $e\mu$ channels. Background yields are predicted directly using simulated MC samples. Object and event selections are applied on simulated signal and background samples. Events passing the selection criteria are used for training a DNN for signal extraction, which categorizes events into multiple classes representing signal or backgrounds. The DNN output is used for obtaining limits, taking into account various systematic uncertainties reflecting Phase-2 conditions.

4.1 Object reconstruction and selection

The objects used in this analysis are reconstructed starting with a dedicated particle flow (PF) algorithm [14] in DELPHES. Particle flow algorithm by definition correlates the basic elements from all detector layers (tracks and clusters) to identify each final-state particle, and combines the corresponding measurements to reconstruct the particle properties on the basis of this identification. Pileup subtraction is applied at the PF candidate level via the so-called PUPPI algorithm [15], that was specifically tuned to reduce the pileup dependence on jets and $p_{\mathrm{T}}^{\mathrm{miss}}$ at 200 average pileup events. Object identification criteria are designed in CMS GEANT4-based [16] full simulation framework, taking into account the Phase-2 conditions. Parametrized object efficiencies and misidentification rates for these identification criteria are derived and implemented in DELPHES. Table 2 summarizes the objects used in this analysis.

Electrons are identified with a boosted decision tree-based algorithm. The medium working point is selected, which has an identification efficiency of 0.8 and mistagging rate of 0.015. Muon identification is an extension of the Run 2 identification by including the Phase-2 muon detector capabilities. The tight working point is selected, which has an identification efficiency of 0.95 and mistagging rate of 0.01. A relative isolation variable I_{rel}^{PF} is defined for the leptons by summing the p_{T} of all PF candidates within a cone of size $\Delta\mathrm{R} = 0.3$ and dividing the sum by the lepton p_{T}. Electrons and muons are required to have relative isolation less than 0.2. The

final state signal leptons are expected to be high-p_T as they are produced in the decay chain of a high mass resonance. Therefore leptons are required to have $p_T > 40\,\text{GeV}$. Pseudorapidity requirements are $|\eta| < 2.4(2.5)$ for muons (electrons).

Jets are reconstructed from the PF candidates using the anti-k_T algorithm with a distance parameter of $\Delta R = 0.4$. A loose identification is applied by imposing criteria on variables related to energy fractions and multiplicities of various PF candidate types clustered in a jet, in order to distinguish physical jets from those arising from calorimetry noise. To prevent overlap between selected jets and leptons, jets found within a cone of $\Delta R < 0.4$ around any of the selected leptons are not considered. Jets are selected to have $p_T > 30\,\text{GeV}$, $|\eta| < 2.4$. Jets originating from the hadronization of bottom quarks are identified using DeepJet [17] algorithm. The jets passing the identification criteria are denoted as b-tagged jets. The medium working point is used with an average b-tagging efficiency of ~ 0.7 and a gluon and light flavor jet mistagging rate of ~ 0.01.

The missing transverse momentum vector $\vec{p}_T^{\,\text{miss}}$ is computed as the negative vector p_T sum of all PF candidates in the event, and its magnitude is denoted as p_T^{miss}.

Table 2: Summary of object definitions and selections.

Object	p_T (GeV)	$\lvert\eta\rvert$	Identification	isolation
Muons	≥ 40	< 2.4	Tight	$I_{PF}^{rel} < 0.2$
Electrons	≥ 40	< 2.5	Medium	$I_{PF}^{rel} < 0.2$
		veto $1.444 < \lvert\eta\rvert < 1.567$		
b-jets	≥ 30	< 2.4	Medium	No e, μ in $\Delta R < 0.4$

4.2 Event selection

Events are required to have exactly two light leptons (electrons or muons) with opposite electric charge. The leading lepton is required to have $p_T > 80\,\text{GeV}$. Dilepton invariant mass $M_{\ell\ell}$ is required to be greater than 110 GeV to suppress contributions from backgrounds with on-shell Z bosons. Missing transverse momentum is required to be $p_T^{\text{miss}} > 80$ GeV to eliminate DY+jets backgrounds (except for the highly boosted dilepton topologies), and partially the $t\bar{t}$ backgrounds. For the highly boosted DY+jets events, jet resolution is poor, leading to visible transverse momentum imbalance. For further suppression of the $t\bar{t}$ backgrounds, events having b-tagged jets are vetoed. Events passing the above criteria are then partitioned into 3 channels based on the lepton flavor configuration as e^+e^-, $\mu^+\mu^-$ and $e^\pm\mu^\mp$. The selection is summarized in Table 3.

Table 3: Event selection and search channels.

Selection variables	Selection criteria		
Number of leptons	$= 2$		
Opposite charge lepton pairs	$= 1, (e^+e^-, \mu^+\mu^-, e^\pm\mu^\mp)$		
Leading lepton p_T	> 80 GeV		
Dilepton invariant mass ($M_{\ell\ell}$)	$> 110\,\text{GeV}$		
Missing transverse momentum (p_T^{miss})	$> 80\,\text{GeV}$		
Number of b-jets	$= 0$		
	Search channels		
Lepton flavors	e^+e^-	$\mu^+\mu^-$	$e^\pm\mu^\mp$

Several kinematic distributions after event selection are shown in Figures 2 and 3 for the $e^\pm\mu^\mp$

and $\mu^+\mu^-$ channels, respectively. The these include the distributions of leading and trailing lepton p_{T}'s; dilepton invariant mass $M_{\ell\ell}$; $p_{\mathrm{T}}^{\mathrm{miss}}$; transverse mass $M_T(\vec{p}_{\mathrm{T}}(\ell\ell), \vec{p}_{\mathrm{T}}^{\mathrm{miss}})$ calculated using the dilepton system and the $\vec{p}_{\mathrm{T}}^{\mathrm{miss}}$; and the stransverse mass M_{T2} [18, 19]. Here, transverse mass is an invariant mass calculated using the transverse components of the visible and invisible systems. Stransverse mass is an extension of transverse mass, which is applicable in cases where $\vec{p}_{\mathrm{T}}^{\mathrm{miss}}$ in an event originates from two invisible particles, e.g. two neutralinos. The computation performs a minimization over all possible partitions of measured $\vec{p}_{\mathrm{T}}^{\mathrm{miss}}$ to find the case where each part is matched closest to each neutralino. These variables are a subset of the list that is used as input to the DNN in the next step of the analysis, described in Section 4.3. They show discriminating behavior between the signal and the SM backgrounds. Signal and background distributions show a similar behavior for both channels. In the $e^{\pm}\mu^{\mp}$ channel, the Drell-Yan+jets background is highly suppressed and has a negligible contribution, leading to lower total background yield and higher signal over background ratios. For the e^+e^- channel, which is not shown here, the distributions, background compositions and yields are very similar to the $\mu^+\mu^-$ channel.

4.3 Signal extraction

Signal sensitivity is further boosted through a DNN. Tensorflow [20] interfaced with the Keras [21] library is used for training the networks. Dedicated training is performed for each signal mass point for each of the e^+e^-, $\mu^+\mu^-$ and $e^{\pm}\mu^{\mp}$ channels to pursue the most optimal signal sensitivity for each case.

Inputs to DNN training consist of kinematic and topological variables that show a good discriminating power between the signal and the backgrounds. They range from low level variables such as lepton transverse momenta to high level variables such as the stransverse mass M_{T2}. In particular, the higher level variables are constructed to characterize the heavy resonances and heavy invisible particles in the signal. Below is the full list of input variables used in the training:

- Kinematical variables: $p_{\mathrm{T}}(\ell_{lead})$, $p_{\mathrm{T}}(\ell_{trail})$, $M(\ell\ell)$, $p_{\mathrm{T}}^{\mathrm{miss}}$, $|\vec{p}_{\mathrm{T}}(\ell\ell) + \vec{p}_{\mathrm{T}}^{\mathrm{miss}}|$, $|\vec{p}_{\mathrm{T}}(\ell\ell) + \vec{p}_{\mathrm{T}}^{\mathrm{miss}}| - p_{\mathrm{T}}(\ell\ell)$, $M_T(\vec{p}_{\mathrm{T}}(\ell\ell), \vec{p}_T^{miss})$, M_{T2}
- Topological variables: $\Delta\phi(\ell,\ell)$, $\Delta\phi(\vec{p}_{\mathrm{T}}^{\mathrm{miss}}, \vec{p}_{\mathrm{T}}(\ell\ell))$, $\Delta\phi(\vec{p}_{\mathrm{T}}^{\mathrm{miss}}, \vec{p}_{\mathrm{T}}(\ell))$, $\Delta R(\ell,\ell)$, $\Delta R(\vec{p}_{\mathrm{T}}(\ell\ell), \vec{p}_{\mathrm{T}}^{\mathrm{miss}})$

Events are categorized into multiple classes representing topologies dominant with the signal or various background processes. The classes for each channel are as follows:

- $\mu\mu$, ee channel (4 classes): signal, $\mathrm{t\bar{t}}$, DY, others (tW and diboson (VV)).
- $e\mu$ channel (3 classes): signal, $\mathrm{t\bar{t}}$, others (single top (tW), diboson (VV) and DY). Since DY has a smaller contribution in this channel, it is not considered as a separate category, but is rather included in the "others" category.

The training outputs a DNN score for each event for each class, which is a single probability value ranging from 0 to 1, where the highest value indicates the event to be consistent with the class. The DNN score distribution for the signal class will be input to the limit calculation.

5 Systematic uncertainties

Table 4 lists the systematic uncertainties considered in this analysis and their effects on inclusive signal and background yields. These systematic variations either only affect the yield rate or affect the shape of the distributions, i.e. having a different effect on each bin. As the analysis does not impose requirements on jets except for vetoing b-jets, jet-related uncertainties have

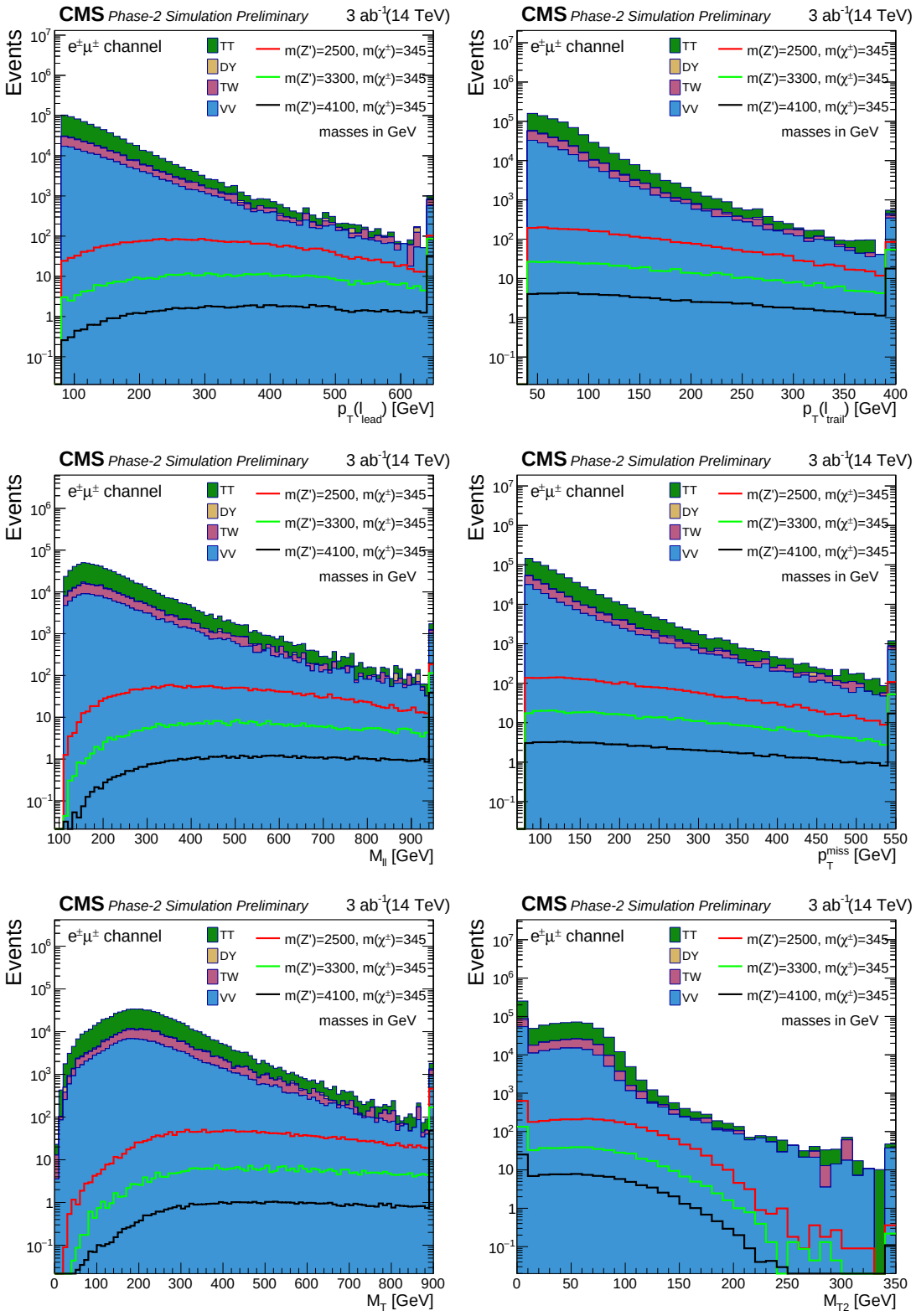

Figure 2: Distributions of several event variables to be input to the DNN, after the event selection for the $e^{\pm}\mu^{\mp}$ channel.

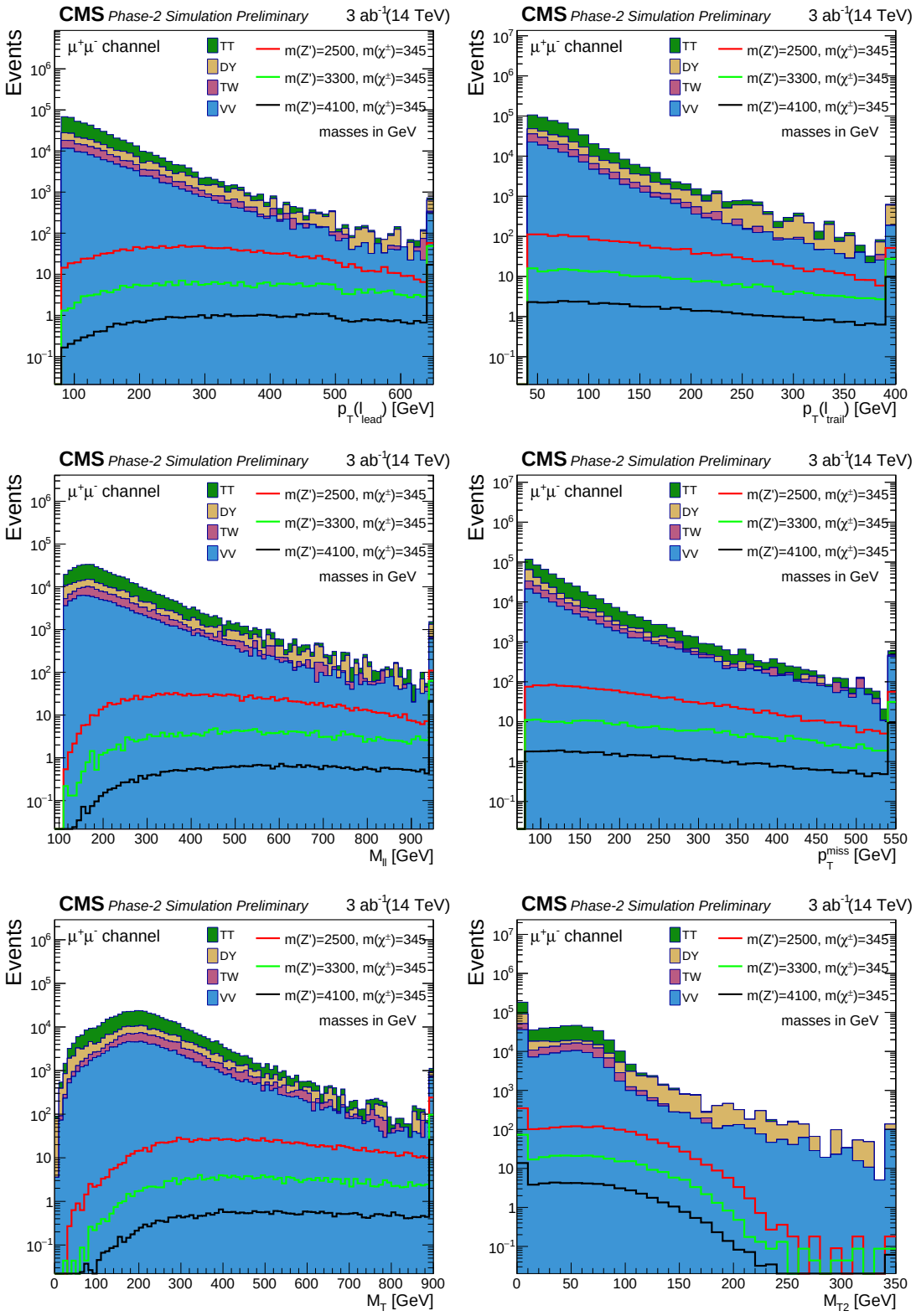

Figure 3: Distributions of several event variables to be input to the DNN, after the event selection for the $\mu^+\mu^-$ channel.

relatively low effects on yields. Since the background estimation is performed directly using MC events, systematic uncertainties that may rise from a potential future data-driven background estimation method are not taken into account. Theoretical uncertainties in the cross sections due to the variation of the QCD scale and parton distribution functions are also considered. The variations are either retrieved from dedicated 14 TeV calculations, or in case not available, Run 2 values are used, by scaling them down by 1/2. QCD scale uncertainties are taken to be $-3.5/+2.3\%$ for $t\bar{t}$+jets, $\pm 2.3\%$ for single top, $\pm 1\%$ for Drell-Yan and $\pm 1.5\%$ for VV processes. For the signal, shape-dependent variation due to QCD scale is computed. PDF uncertainties are considered for the top processes, having a rate effect of $\pm 4\%$ for $t\bar{t}$+jets and $-5.7/+3.5\%$ for single top. This prescription, referred to as the "YR18 scenario", was introduced in the CERN Yellow Report for BSM physics at HL-LHC [22]. Statistical uncertainties are assumed for a future scenario having sufficient resources to produce very large MC samples with MC event weights corresponding to 1.

Table 4: List of systematic uncertainties applied in this analysis, their values and their effects on signal and total background yields. Inclusive effects on yields are quoted for the signal region, considering the most conservative values from e^+e^-, $\mu^+\mu^-$ and $e^\pm\mu^\mp$ channels.

Uncertainty source	Input effect (±%)	Variation	Effect on signal (±%)	Effect on total BG (%)
Jet energy scale (JES)	0.4–3	shape	negligible	≤ 0.55
$p_{\mathrm{T}}^{\mathrm{miss}}$ (JES propagation)	0.4–3	shape	negligible	≤ 0.2
b-tagging	1–2	shape	negligible	≤ 1.25
Lepton identification	0.5	rate	1	1
Luminosity	1	rate	1	1
Theory uncertainties: QCD scale and PDFs				

6 Results and interpretation

Figure 4 shows the DNN discriminant scores for the signal class for an example signal point with a Z′ mass of 2500 GeV and a $\tilde{\chi}_1^\pm$ mass of 1095 GeV for the e^+e^-, $\mu^+\mu^-$ and $e^\pm\mu^\mp$ channels. Effect of statistical and systematical uncertainties are also displayed. The DNN performance is similar for all three channels, however signal sensitivity is better in the $e^\pm\mu^\mp$ channel presumably due to inherently smaller contribution from the Drell-Yan+jets background.

The dedicated signal class DNN score for each signal point is used to calculate limits through a binned maximum likelihood fit, using the binning shown in Figure 4 for the three individual channels and for their combination. Experimental and theoretical systematic uncertainties are considered as the nuisance parameters of the likelihood functions, for which log-normal a prior distributions are assumed. Figure 5 shows the expected upper limits at 95% confidence level on the $pp \to Z'$ production cross section computed using the CLs technique [23, 24], for the leptophobic Z′ scenario in the $Z' \to \tilde{\chi}_1^+\tilde{\chi}_1^+ \to W^+\tilde{\chi}_1^0 W^-\tilde{\chi}_1^0 \to \ell^+\nu\tilde{\chi}_1^0\ell^-\nu\tilde{\chi}_1^0$ decays. Limits are shown in the chargino mass versus Z′ mass plane for 3 ab^{-1} of integrated luminosity for the e^+e^-, $\mu^+\mu^-$ and $e^\pm\mu^\mp$ channels and the combination of these three channels. The Z′ width has the approximate value of 1.5% of the Z′ mass. The neutralino mass is considered to be half the chargino mass and the $Z' \to \tilde{\chi}_1^+\tilde{\chi}_1^- \to W^+\tilde{\chi}_1^0 W^-\tilde{\chi}_1^0$ branching ratio is considered to be equal to 1. The $\mu^+\mu^-$ and e^+e^- channels have similar sensitivity while the $e^\pm\mu^\mp$ channel shows better sensitivity due to having twice the expected signal and negligible Drell-Yan+jets background yields. As a consequence, the combined limits are mostly driven by the $e^\pm\mu^\mp$ channel.

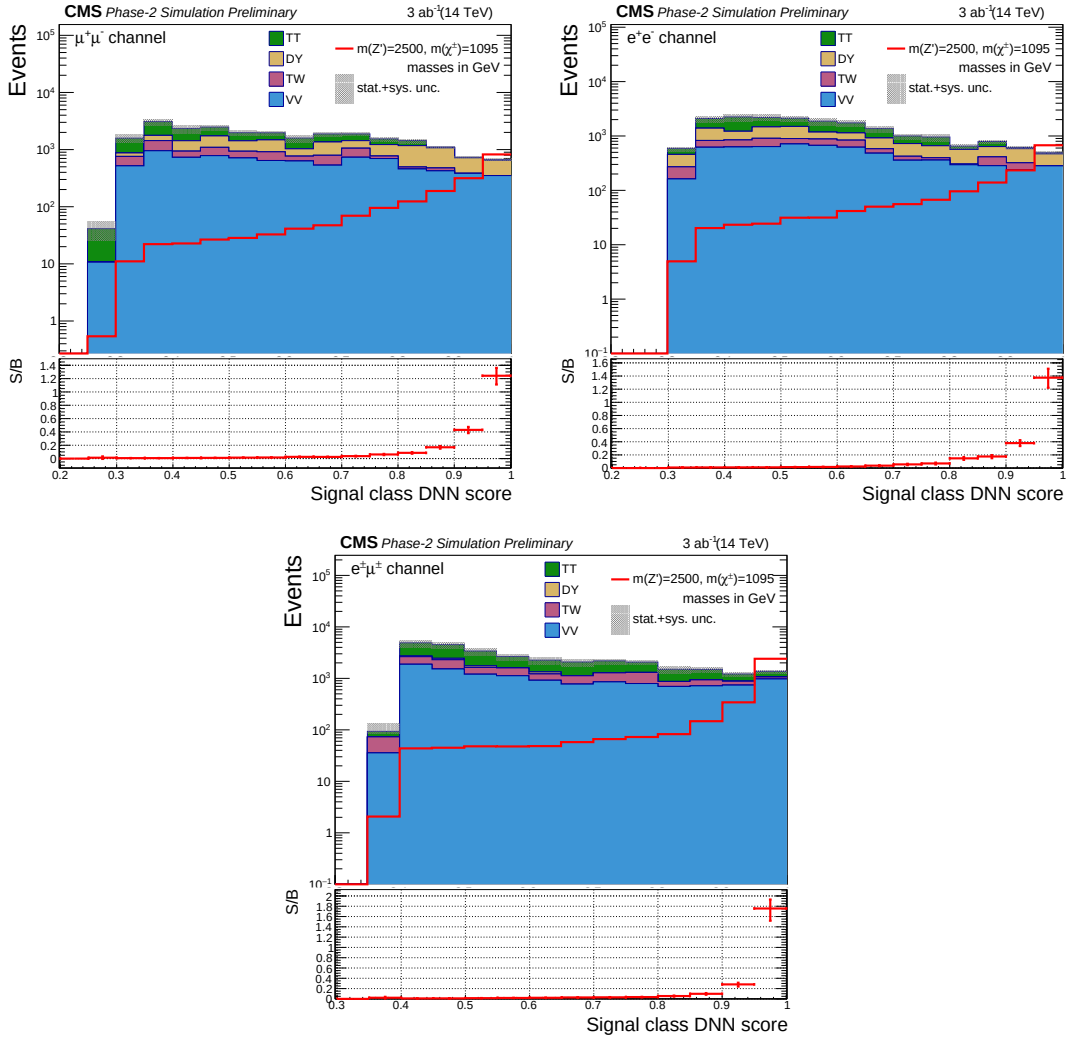

Figure 4: DNN discriminant score distributions for the signal class in the $\mu^+\mu^-$ (top left), e^+e^- (top right) and $e^\pm\mu^\mp$ (bottom) channels for a signal point with a Z′ mass of 2500 GeV and a $\tilde{\chi}_1^\pm$ mass of 1095 GeV. Effect of statistical and systematical uncertainties are also shown. The bottom panel in each plot displays the signal over background ratios.

7 Summary

A study was performed to predict the sensitivity of the HL-LHC to leptophobic Z′ decaying to two charginos, which subsequently decay to W bosons and neutralinos. Leptophobic Z′ are predicted in various extensions of supersymmetry. This is the first study of this model and process at the LHC. An analysis was designed in the dilepton plus missing transverse momentum final state, in the ee, $\mu\mu$ and $e\mu$ channels and performed on events simulated with the LH-LHC and Phase-2 CMS detector conditions. A deep neural network was employed to enhance signal sensitivity. The analysis was interpreted using simplified model spectra featuring the production and decay process of the leptophobic Z′ derived from the U(1)′ extension of the minimal supersymmetric standard model. Upper limits on the Z′ production cross section were presented in the Z′ mass versus chargino mass plane, with $m(\tilde{\chi}_1^0) = 2m(\tilde{\chi}_1^0)$ and Z′ width assumed to be 1.5% of the Z′ mass. With an integrated luminosity of 3 ab^{-1}, the combined analysis will be able to exclude Z′ masses up to 4.4 TeV for decays into $Z' \to \tilde{\chi}^+\tilde{\chi}^- \to W^+\tilde{\chi}_1^0 W^-\tilde{\chi}_1^0$

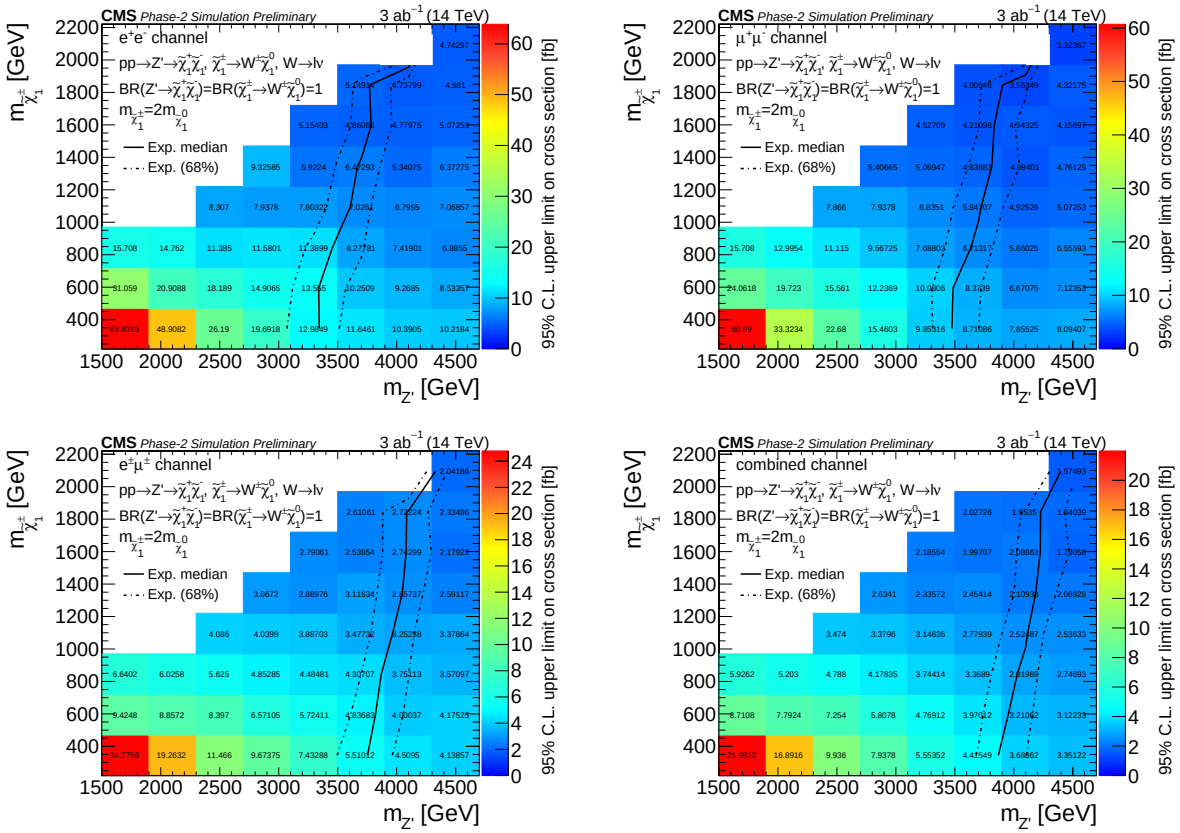

Figure 5: The expected upper limits at 95% confidence level computed with the CLs method on the $pp \to Z'$ production cross sections are shown for e^+e^- (top left), $\mu^+\mu^-$ (top right), $e^\pm\mu^\mp$ (bottom left) and combined (bottom right) channels. Limits are calculated from the process $Z' \to \tilde{\chi}_1^+\tilde{\chi}_1^- \to W^+\tilde{\chi}_1^0 W^-\tilde{\chi}_1^0 \to \ell^+\tilde{\chi}_1^0\ell^-\tilde{\chi}_1^0$. Z' width is considered to be approximately 1.5% of the Z' mass, neutralino mass is considered to be half the chargino mass and the $Z' \to \tilde{\chi}_1^+\tilde{\chi}_1^- \to W^+\tilde{\chi}_1^0 W^-\tilde{\chi}_1^0$ branching ratio is considered to be equal to 1. Median expected CLs upper limits (95% CL) on Z' production cross sections are shown in the colored grid. The solid line denotes the median exclusion and the dashed lines denote the 68% interval.

with a branching ratio of 1. However, the excluded Z' masses will be smaller in full models with complete sparticle spectra, which will have lower branching ratios.

References

[1] CMS Collaboration, "Technical Proposal for the Phase-II Upgrade of the CMS Detector", CMS Technical Proposal CERN-LHCC-2015-010. LHCC-P-008. CMS-TDR-15-02, 2015.

[2] ATLAS Collaboration, "Search for high-mass dilepton resonances using 139 fb^{-1} of pp collision data collected at $\sqrt{s}$ =13 TeV with the ATLAS detector", *Phys. Lett. B* **796** (2019) 68–87, doi:10.1016/j.physletb.2019.07.016, arXiv:1903.06248.

[3] CMS Collaboration, "Search for resonant and nonresonant new phenomena in high-mass dilepton final states at $\sqrt{s}$ = 13 TeV", *JHEP* **07** (2021) 208, doi:10.1007/JHEP07(2021)208, arXiv:2103.02708.

[4] CMS Collaboration, "Search for high mass dijet resonances with a new background prediction method in proton-proton collisions at $\sqrt{s} = 13$ TeV", *JHEP* **05** (2020) 033, doi:10.1007/JHEP05(2020)033, arXiv:1911.03947.

[5] J. Y. Araz, G. Corcella, M. Frank, and B. Fuks, "Loopholes in Z' searches at the LHC: exploring supersymmetric and leptophobic scenarios", *JHEP* **02** (2018) 092, doi:10.1007/JHEP02(2018)092, arXiv:1711.06302.

[6] M. Frank, Y. Hiçyılmaz, S. Moretti, and O. Özdal, "E_6 motivated UMSSM confronts experimental data", *JHEP* **05** (2020) 123, doi:10.1007/JHEP05(2020)123, arXiv:2004.01415.

[7] M. Frank, Y. Hiçyılmaz, S. Moretti, and O. Özdal, "Leptophobic Z' bosons in the secluded UMSSM", *Phys. Rev. D* **102** (2020), no. 11, 115025, doi:10.1103/PhysRevD.102.115025, arXiv:2005.08472.

[8] CMS Collaboration, "The CMS Experiment at the CERN LHC", *JINST* **3** (2008) S08004, doi:10.1088/1748-0221/3/08/S08004.

[9] CMS Collaboration, "The Phase-2 Upgrade of the CMS Tracker", CMS Technical Design Report CERN-LHCC-2017-009. CMS-TDR-014, 2017.

[10] CMS Collaboration, "The Phase-2 Upgrade of the CMS Barrel Calorimeters Technical Design Report", CMS Technical Design Report CERN-LHCC-2017-011. CMS-TDR-015, 2017.

[11] CMS Collaboration, "The Phase-2 Upgrade of the CMS Endcap Calorimeter", CMS Technical Design Report CERN-LHCC-2017-023. CMS-TDR-019, 2017.

[12] CMS Collaboration, "The Phase-2 Upgrade of the CMS Muon Detectors", CMS Technical Design Report CERN-LHCC-2017-012. CMS-TDR-016, 2017.

[13] CMS Collaboration, "Expected performance of the physics objects with the upgraded CMS detector at the HL-LHC", Technical Report CMS-NOTE-2018-006. CERN-CMS-NOTE-2018-006, 2018.

[14] CMS Collaboration, "Particle-flow reconstruction and global event description with the CMS detector", *JINST* **12** (2017), no. 10, P10003, doi:10.1088/1748-0221/12/10/P10003, arXiv:1706.04965.

[15] D. Bertolini, P. Harris, M. Low, and N. Tran, "Pileup per particle identification", *JHEP* **10** (2014) 059, doi:10.1007/JHEP10(2014)059, arXiv:1407.6013.

[16] GEANT4 Collaboration, "GEANT4–a simulation toolkit", *Nucl. Instrum. Meth. A* **506** (2003) 250–303, doi:10.1016/S0168-9002(03)01368-8.

[17] CMS Collaboration Collaboration, "B-tagging performance of the CMS Legacy dataset 2018.",.

[18] C. G. Lester and D. J. Summers, "Measuring masses of semiinvisibly decaying particles pair produced at hadron colliders", *Phys. Lett. B* **463** (1999) 99–103, doi:10.1016/S0370-2693(99)00945-4, arXiv:hep-ph/9906349.

[19] A. Barr, C. Lester, and P. Stephens, "m(T2): The Truth behind the glamour", *J. Phys. G* **29** (2003) 2343–2363, doi:10.1088/0954-3899/29/10/304, arXiv:hep-ph/0304226.

[20] M. Abadi et al., "TensorFlow: Large-scale machine learning on heterogeneous systems", 2015. Software available from tensorflow.org. https://www.tensorflow.org/.

[21] F. Chollet et al., "Keras". https://keras.io, 2015.

[22] X. Cid Vidal et al., "Report from Working Group 3: Beyond the Standard Model physics at the HL-LHC and HE-LHC", *CERN Yellow Rep. Monogr.* **7** (2019) 585–865, doi:10.23731/CYRM-2019-007.585, arXiv:1812.07831.

[23] T. Junk, "Confidence level computation for combining searches with small statistics", *Nucl. Instrum. Meth. A* **434** (1999) 435–443, doi:10.1016/S0168-9002(99)00498-2, arXiv:hep-ex/9902006.

[24] A. L. Read, "Presentation of search results: The CL(s) technique", *J. Phys. G* **28** (2002) 2693–2704, doi:10.1088/0954-3899/28/10/313.